

RESEARCH ARTICLE

SOLAR CELLS

Efficient, stable silicon tandem cells enabled by anion-engineered wide-bandgap perovskites

Daehan Kim^{1*}, Hee Joon Jung^{2*}, Ik Jae Park^{3*}, Bryon W. Larson⁴, Sean P. Dunfield^{4,5}, Chuanxiao Xiao⁴, Jekyung Kim¹, Jinhui Tong⁴, Passarut Boonmongkolras¹, Su Geun Ji³, Fei Zhang⁴, Seong Ryul Pae¹, Minkyu Kim¹, Seok Beom Kang⁶, Vinayak Dravid², Joseph J. Berry^{4,7,8}, Jin Young Kim^{3†}, Kai Zhu^{4†}, Dong Hoe Kim^{4,6†}, Byungha Shin^{1†}

Maximizing the power conversion efficiency (PCE) of perovskite/silicon tandem solar cells that can exceed the Shockley-Queisser single-cell limit requires a high-performing, stable perovskite top cell with a wide bandgap. We developed a stable perovskite solar cell with a bandgap of ~1.7 electron volts that retained more than 80% of its initial PCE of 20.7% after 1000 hours of continuous illumination. Anion engineering of phenethylammonium-based two-dimensional (2D) additives was critical for controlling the structural and electrical properties of the 2D passivation layers based on a lead iodide framework. The high PCE of 26.7% of a monolithic two-terminal wide-bandgap perovskite/silicon tandem solar cell was made possible by the ideal combination of spectral responses of the top and bottom cells.

Perovskite photovoltaic (PV) technology has advanced substantially, with the present record efficiency for single-junction devices reaching >25% (1–4). One of the most promising strategies for commercializing these devices is to apply a perovskite top cell in tandem with a Si bottom cell to reach ultrahigh efficiency beyond the Shockley-Queisser limit for single-junction devices (5). Since the report of a two-terminal (2T) perovskite/Si tandem solar cell by Mailoa *et al.* (6), several groups have reported encouraging results (7–10). Most of the studies on perovskite/Si tandem solar cells have perovskite absorbers with the conventional bandgap of 1.5 to 1.6 eV, but the ideal bandgap for the tandem configuration is ~1.67 to 1.75 eV for the top cell and 1.12 eV for the bottom cell, which, fortuitously, is the Si bandgap (11). Although some of the reported perovskite/Si tandem devices have used a wide-bandgap perovskite (near 1.7 eV), the power conversion efficiencies (PCEs) reported have been ≤25% (8).

The bandgap of perovskites can be tuned by (partial) replacement of iodine anions with bromine or chlorine. However, the replacement of I with Br by more than ~20%, which is necessary to enlarge the bandgap to ~1.7 eV, leads to stability issues under illumination through phase separation that forms I-rich and Br-rich structures (12). One approach to stabilize the perovskite is to create a two-dimensional (2D) phase in which sheets of [PbX₆]^{2−} octahedra are separated by an excess number of long-chain (or aromatic) molecules that act as a passivation agent (13–17). Common long-chain or aromatic molecule-based 2D additives include *n*-butylammonium iodide (n-BAI) and phenethylammonium iodide (PEAI) (13, 15). For example, Wang *et al.* have used n-BAI as a 2D additive and demonstrated an extended lifetime of up to 1000 hours under illumination (13). Kim *et al.* have developed a wide-bandgap perovskite with PEAI as a 2D additive and demonstrated successful integration into perovskite/Cu(In,Ga)Se₂ tandem solar cells (17). Formation of passivation layers induced by these 2D additives improved efficiency, particularly the open-circuit voltage (*V*_{OC}); however, excessive incorporation of 2D-forming molecules often reduced the fill factor (FF) because of their electrically insulating nature. Thus, the concentration of the added 2D molecules has been limited to ~1 mol % in the precursor solutions.

Most of the recent studies have focused on the cation components of the 2D additives rather than focusing on the anions. We developed a 2D-3D mixed wide-bandgap (1.68 eV) perovskite using a mixture of thiocyanate (SCN) with the more-conventional choice, iodine. Through a careful application of atomic-resolution trans-

mission electron microscopy (TEM), we demonstrated that electrical and charge transport properties as well as the physical location of 2D passivation layers can be controlled with anion engineering of the 2D additives. Moreover, we can use this approach to extend light stability and to improve device performance. For a perovskite device, we achieved a PCE of 20.7% that retained >80% of its initial efficiency after 1000 hours of continuous illumination in working conditions. For a monolithic 2T perovskite/Si tandem solar cell, the champion 2T tandem device achieved a PCE of 26.7%.

Anion engineering of wide-bandgap solar cells

The wide-bandgap (1.68 eV) perovskite used in this study was (FA_{0.65}MA_{0.2}CS_{0.15})Pb(I_{0.8}Br_{0.2})₃. An additional 2 mol % of Pb(SCN)₂ was added to the perovskite precursor solution to accelerate the 3D perovskite grain growth (17). To form a 2D phase, PEA-based additives had an anion component mixture of I and SCN with various ratios of SCN/(SCN + I), ranging from 0 to 100%. Solar cells were fabricated with an indium tin oxide (ITO)/poly(triaryl amine) (PTAA)/perovskite/C₆₀/bathocuproine (BCP)/Ag device structure (fig. S1). Representative current density-voltage (*J*-*V*) curves of devices with three different SCN/(SCN+I) ratios—0, 75, and 100% (Fig. 1A)—show that the highest *V*_{OC} was from the pure PEAi and the highest *J*_{SC} was from the pure PEASCN, but the highest performance was from the mixed anion sample.

We further investigated the influence of the anion composition in the 2D additives on the PV parameters using a series of samples with different ratios of SCN to (SCN + I). In all of the samples, the concentration of the 2D additives added to the precursor solutions was fixed at 2 mol %, which was determined by the device optimization (fig. S2). Increasing SCN/(SCN + I) decreased *V*_{OC} but improved *J*_{SC} and FF (Fig. 1B). The variation of *V*_{OC} was not caused by slight changes in the optical bandgap of the different perovskite films (fig. S3). A compromise between the PV parameters produced the highest efficiency with the additives of 75% SCN, in other words, PEA(I_{0.25}SCN_{0.75}). Thus, SCN promoted the *J*_{SC} and FF of the devices, but iodine seemed essential in defect passivation that led to higher *V*_{OC}.

The *J*-*V* curve of the champion cell with the PEA(I_{0.25}SCN_{0.75}) additive (Fig. 1C) led to a 20.7% PCE and a stabilized power output (SPO) >20%. The external quantum efficiency (EQE) shown in fig. S4A from the same device showed a minimal mismatch with the *J*_{SC} from the *J*-*V* scan (<4%) and negligible *J*-*V* hysteresis between the different scan directions (fig. S4B). For a long-term stability test of the devices under continuous illumination in an N₂-filled environment (18), samples without any encapsulation were subjected to *J*-*V* measurements every 30 min (Fig. 1D). Compared with

¹Department of Materials Science and Engineering, Korea Advanced Institute of Science and Technology (KAIST), Daejeon 34141, Republic of Korea. ²Department of Materials Science and Engineering, Northwestern University, Evanston, IL 60208, USA. ³Department of Materials Science and Engineering, Seoul National University, Seoul 08826, Republic of Korea. ⁴National Renewable Energy Laboratory, Golden, CO 80401, USA. ⁵Materials Science and Engineering Program, University of Colorado Boulder, Boulder, CO 80309, USA. ⁶Department of Nanotechnology and Advanced Materials Engineering, Sejong University, Seoul 05006, Republic of Korea. ⁷Department of Physics, University of Colorado Boulder, Boulder, CO 80309, USA. ⁸Renewable and Sustainable Energy Institute, University of Colorado Boulder, Boulder, CO 80309, USA.

*These authors contributed equally to this work.

†Corresponding author. Email: jykim.mse@snu.ac.kr (J.Y.K.); kai.zhu@nrel.gov (K.Z.); donghoe.k@sejong.ac.kr (D.H.K.); byungha@kaist.ac.kr (B.S.)

the samples with pure PEA and PEASCN additives, the mixed anion additive that led to the champion device exhibited much-improved stability—80% of the initial efficiency was maintained even after 1000 hours of continuous illumination (J - V curves acquired during the stability tests are shown in fig. S5). A greatly extended light stability of a wide-bandgap perovskite (~ 1.67 eV) has recently been demonstrated by McGehee *et al.* (19) that uses a tri-halide alloy (mixture of Cl, Br, and I). The extended stability in that case has been attributed to markedly improved structural and optoelectronic properties (enhanced carrier lifetime and mobility and reduced defect density) of the perovskite. We also observed improved structural and optoelectronic properties via the optimized anion-engineered 2D additive, as discussed later in this work.

Structural characterization

We explored the roles of different PEA-based additives on the device operation through extensive structural analysis. The films were examined by scanning electron microscopy (SEM) (Fig. 2, A to C). The average grain size was larger for the SCN-based PEA source than that of the pure PEA additive, which confirmed the previous reports on the enhanced grain growth promoted by SCN molecules (17, 20). However, compared with the perovskite film with only $\text{Pb}(\text{SCN})_2$ (fig. S6B), PEA apparently suppressed grain growth, which limited the average grain size to less than ~ 500 nm. Consistent with the SEM results, x-ray diffrac-

tion (XRD) (Fig. 2D) revealed that films with the PEASCN additive were more crystalline than a film with the PEA additive, as determined by the full width at half maximum of the XRD peaks (fig. S7). The PbI_2 phase peak was observed in all of the films and was strongest for the pure PEA film. In addition to the well-defined grains of the 3D perovskite, patches of a new phase with a bright SEM image contrast (indicating a more insulating nature than the darker 3D perovskite grains) were observed. Most of these patches were preferentially located at grain boundaries instead of residing directly over grains.

To probe the chemical and structural properties of the new phase coexisting with the 3D perovskite host, we performed cross-sectional TEM studies including atomic-resolution scanning TEM (STEM) images. Figure 2, E and F, presents bright-field and high-resolution TEM images of the $\text{PEA}(\text{I}_{0.25}\text{SCN}_{0.75})$ sample that show the layered structure (2D phase) located at the grain boundary. The interplanar d-spacing of the 2D phase of 7.1 Å measured from the high-resolution image (Fig. 2G) was also confirmed by selected-area diffraction in fig. S8B. High-angle annular dark-field (HAADF) and annular bright-field (ABF) STEM images (Fig. 2, H and I) helped identify the atomic configuration of the 2D phase. HAADF can be interpreted as Z-contrast imaging, which renders a heavier element brighter with no contrast reversals (21, 22), and ABF phase-contrast imaging visualizes weak-phase objects of low-Z atoms such as hydrogen and oxygen (23). As the dark

contrast of light atoms in the ABF was not pronounced enough to be well resolved, the contrast of the ABF was reversed to yield a reverse ABF (RABF), in which light atoms now appeared bright on the dark background.

The measured d-spacing values of the 2D phase were 2.3 and 7.1 Å along the in-plane and out-of-plane directions, respectively. Notably, these values are near the planar spacings of PbI_2 (110) and (001), respectively, with just 1 and 1.7% expansion compared with the (110) and (001) planar spacing of pure PbI_2 (JCPDS-73-1750, Trigonal P3m1, $a = 4.5570$ Å and $c = 6.9790$ Å). This result suggested that the 2D phase was primarily PbI_2 . Direct comparisons of the atomic-scale structures of pure PbI_2 and those of our 2D phase are presented in fig. S9. A subtle distinction between our 2D phase and the pure PbI_2 is the observation of interlayer atomic or molecular dopants in the RABF image (and also in the HAADF image, although the contrast is more diffuse) of our 2D phase, whereas such contrast was absent in the pure PbI_2 . These data suggest that the interlayer dopants were likely SCN or Cs, and the incorporation of the interlayer dopants must be at least partially responsible for the lattice expansion.

To further confirm the structural origin of our 2D phase, we performed STEM simulations of PbI_2 and PEA_2PbI_4 (fig. S10), which illustrated much better matching of the real high-resolution STEM images with the simulations of PbI_2 compared with PEA_2PbI_4 . Energy-dispersive spectroscopy analysis of a surface 2D phase (fig. S11) revealed that the 2D phase

Fig. 1. Device performance and stability under illumination of perovskite solar cells with different 2D additives. (A) Representative J - V curves of perovskite solar cells with different incorporated additives. Precursor solutions consisted of a mixture of FAI, MABr, PbI_2 , PbBr_2 , and CsI to form a stoichiometric 3D perovskite + Pb

$(\text{SCN})_2$ + $\text{PEA}(\text{I}_{1-x}\text{SCN}_x)$, where $x = 0, 0.75$, or 1. (B) Statistics of PV parameters with various ratios of SCN to (SCN + I) in the 2D additives ($x = 0, 0.25, 0.5, 0.75$, or 1). (C) J - V curve of the champion wide-bandgap perovskite solar cell [$\text{PEA}(\text{I}_{0.25}\text{SCN}_{0.75})$]. (D) Long-term stability (PCE normalized over the initial efficiency) of perovskite devices under light illumination without encapsulation.

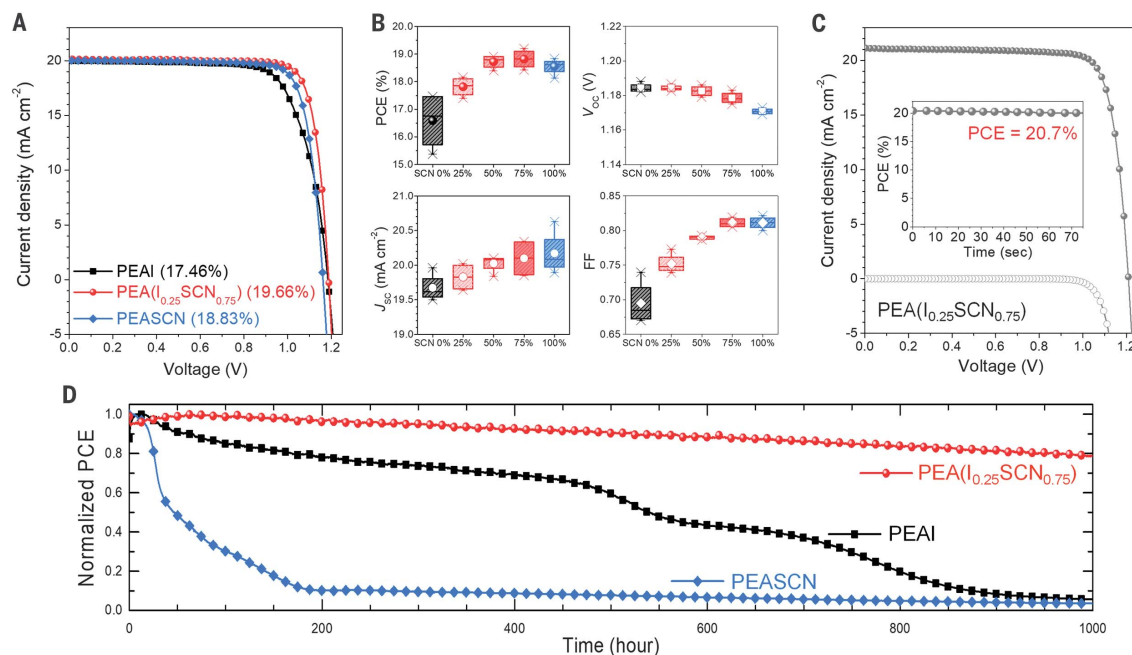


Fig. 2. Structural properties of perovskite films. (A to D) Plan-view SEM images [(A) to (C)] and XRD patterns (D) of perovskite films formed with different 2D additives. a.u., arbitrary unit. **(E to G)** TEM images from $\text{PEA}(\text{I}_{0.25}\text{SCN}_{0.75})$ showing the 2D phase at the grain boundary (GB) of the 3D perovskite host. The inset of (G) shows a fast Fourier transform pattern. **(H to K)** Atomic-scale STEM images [(H) to (J)] and the schematic (K) of the atomic structure of the 2D phase (PbI_2 with interlayer dopants). Results from the $\text{PEA}(\text{I}_{0.25}\text{SCN}_{0.75})$ sample, (B) and (E to K), are marked by red boxes.

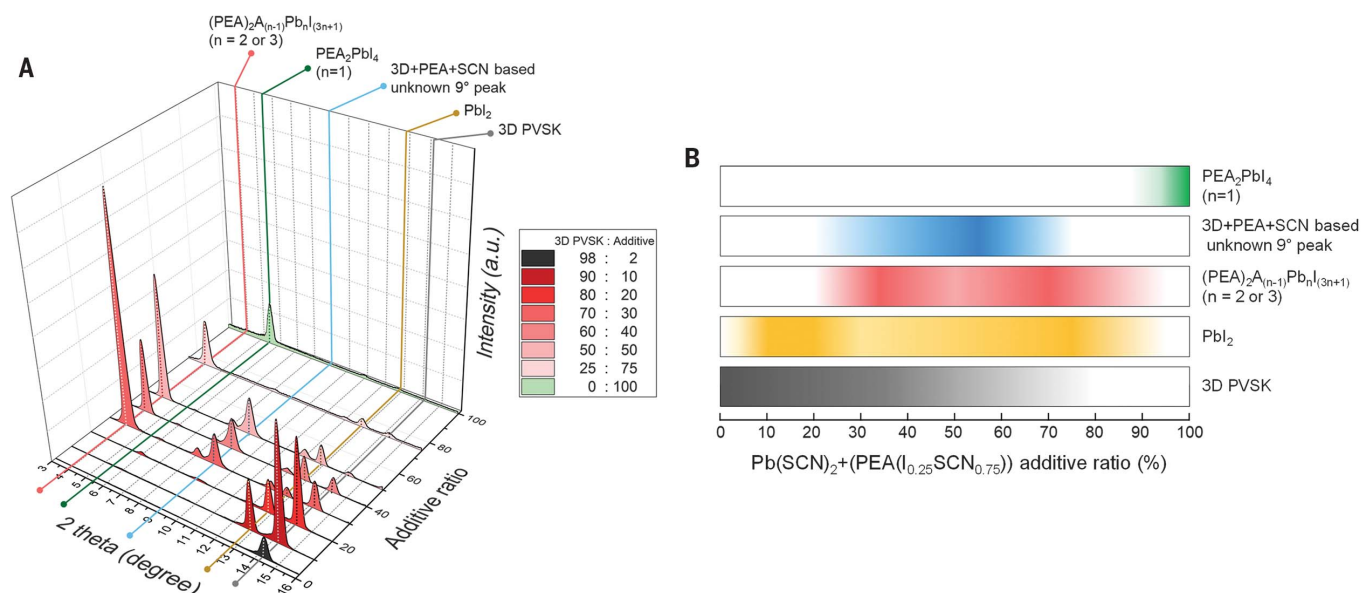
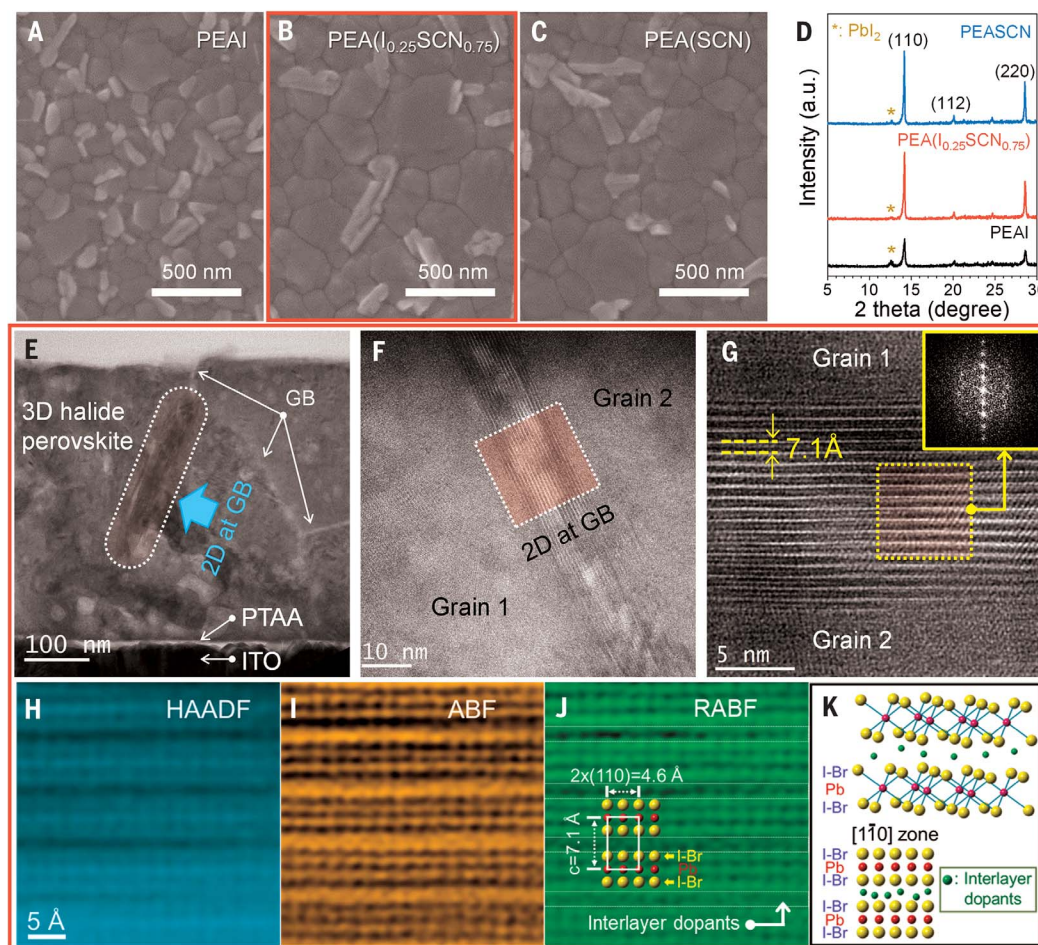


Fig. 3. Series of XRD of films formed with varying ratios of 2D additive to 3D perovskite precursor chemicals. (A) XRD patterns with differing ratios (mole %) of 2D additives, i.e., $\text{Pb}(\text{SCN})_2 + \text{PEA}(\text{I}_{0.25}\text{SCN}_{0.75})$, to 3D perovskite precursors. **(B)** Color-coded visualization of different phases formed. The intensity of the color represents the strength of the corresponding XRD peak. The white background in each row represents the absence of the phase.

contained Pb, I, Br, N, and Cs, which confirms that it is PbI_2 -based with the inclusion of SCN, Br, and Cs. The sample with only the $\text{Pb}(\text{SCN})_2$ additive without PEA appeared to have only surface 2D phases, whereas the $\text{PEA}(\text{I}_{0.25}\text{SCN}_{0.75})$ sample had a 2D phase both on the surface and at grain boundaries (figs. S11 and S12). Previous studies have shown segregation of PEA molecules at grain boundaries of perovskites and their passivation effect (24). The large size of PEA is only readily hosted at grain boundaries. For the grain boundary with 2D phase present, the space between the grain and the 2D phase is where we expect PEA molecules to reside. Thus, we speculate that PEA not only acted as a passivation agent itself, but that it also assisted the passivation of grain boundaries by preferentially placing the PbI_2 -based 2D phase.

Previous studies have identified 2D passivation layers derived from PEA (or BAI) as PEA_2PbI_4 (or BAI_2PbI_4), a low-dimensional perovskite, $\text{A}_2\text{A}'_{(n-1)}\text{B}_n\text{X}_{(3n+1)}$, with $n = 1$ (13). An obvious difference between these reports and our work is the inclusion of SCN in the anion component of the 2D additives. To elucidate reaction pathways under our precursor chemistry, we carried out a series of XRD measurements on perovskite films formed by precursor solutions where 3D perovskite chemicals (FAI, MABr, CsI, PbBr_2 , and PbI_2) were mixed with

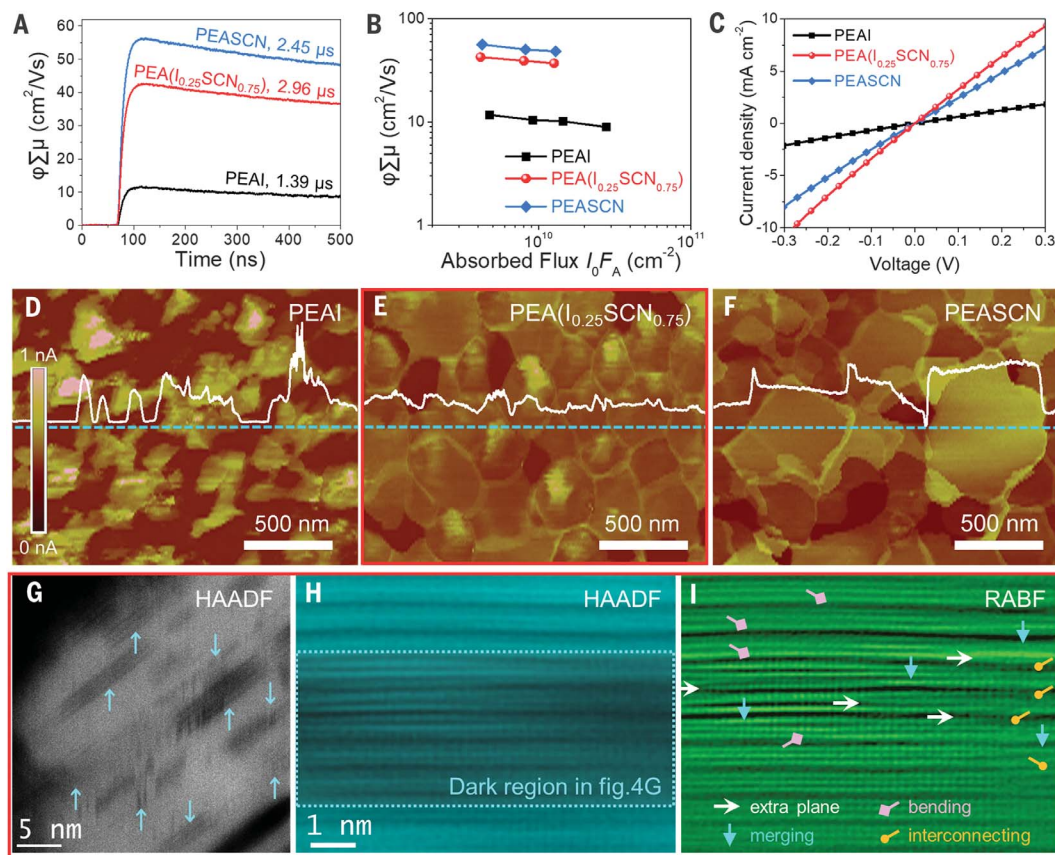
2D additives [$\text{Pb}(\text{SCN})_2$ and $\text{PEA}(\text{I}_{0.25}\text{SCN}_{0.75})$] (Fig. 3). We investigated a wide range of the relative concentrations of 2D additives to the 3D perovskite chemicals—from 2 mol %, which was the condition used to yield films for photovoltaic devices, to 100 mol %.

As anticipated, in the film produced with only the 2D additive chemicals (100 mol %), only the PEA_2PbI_4 phase was present. But, when 3D perovskite precursor chemicals were added (25% was the minimum mole % of the 3D perovskite chemicals in our study), the PEA_2PbI_4 phase was suppressed and new phases—an unidentified 9° peak, low-dimensional perovskite ($\text{PEA})_2\text{A}_{(n-1)}\text{Pb}_n\text{I}_{(3n+1)}$ ($n = 2$ or 3), PbI_2 , and 3D perovskite—began to form. Upon reducing the relative concentration of the 2D additives to below 20%, all of these phases, except PbI_2 and 3D perovskite, disappeared. Notably, upon reducing the ratio of the 2D additives from 30 to 20%, the low-dimensional perovskite peak disappeared while the PbI_2 peak intensified, which suggests that as these two phases compete for Pb and I, PbI_2 dominates over the low-dimensional phase. Preferential formation of PbI_2 over the other secondary phases, which was more pronounced with the reducing concentration of the 2D additives, agreed well with the TEM results presented in Fig. 2.

Similar XRD measurements were performed on perovskite films with pure PEA or PEASCN

(fig. S13). A similar trend was observed in terms of the appearance and disappearance of different phases with the 2D additive ratio. However, PEA_2PbI_4 was absent with the full PEASCN (it formed only when PEA was present in the precursor solutions), which indicates the difficulty of forming a PEA-based 2D phase with SCN anions. Also, at the same mole % of the 2D additives, the relative intensity of the PbI_2 was larger with the increasing ratio of I to SCN in the PEA source (fig. S14). We believe that the more-facile formation of PbI_2 with an increasing ratio of I to SCN accounted for the trend of the V_{OC} change in the devices shown in Fig. 1B. As revealed by TEM, PbI_2 -based 2D layers exist at grain boundaries. These layers could become thicker, cover wider areas of grain boundaries, or do both of these things with the increasing ratio of I to SCN. This process led to more-effective passivation and a larger V_{OC} . Both PEA molecules and the PbI_2 -based 2D phase at the grain boundaries, the formation of which we speculate is catalyzed by the presence of PEA, should contribute to passivation. The positive role of PbI_2 residing at grain boundaries—that is improving V_{OC} —has been well-documented in the literature (25). However, the insulating nature of PbI_2 , especially when present in large quantities, would likely decrease FF, as observed in our device results (26).

Fig. 4. Electrical properties of perovskite films and the observation of planar defects in 2D passivation layers. (A) Photoconductivity transient of perovskite films measured by time-resolved microwave conductivity. (B) Excitation intensity dependence of the photoconductivity in the absorbed flux ($I_0 F_A$) range from 4.0×10^9 to $3.0 \times 10^{10} \text{ cm}^{-2}$. (C) Vertical J - V curve of ITO/perovskite/Au. (D to F) C-AFM maps. (G) HAADF image revealing the formation of regions with defects (dark contrast indicated by arrows) within the 2D phase in the $\text{PEA}(\text{I}_{0.25}\text{SCN}_{0.75})$ film. (H and I) Atomically resolved HAADF and RABF images of the 2D phase. Planar defects such as insertion of extra planes (edge dislocation-like) and the merging or splitting and bending of layers are indicated. Different types of defects are marked by arrows in different colors in (I).



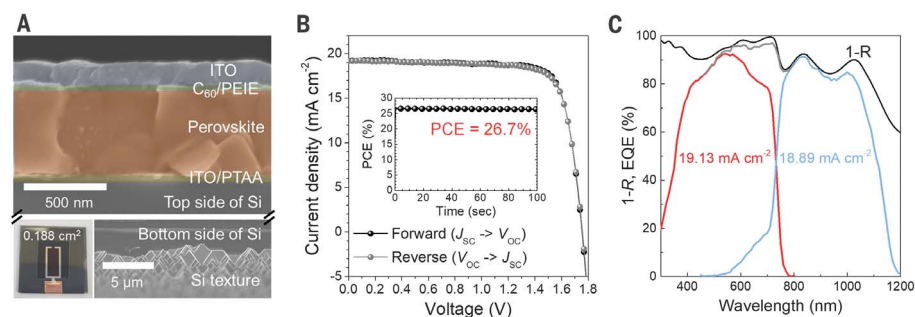


Fig. 5. Structure and photovoltaic performance for the 2T perovskite/Si tandem device. (A) Cross-sectional SEM image showing the full device structure of our 2T perovskite/Si tandem device. The inset shows a photograph of a tandem solar cell. (B) J - V curve of the champion perovskite/Si 2T tandem device with stabilized power output shown in the inset. (C) EQE and 1- R spectrum of the tandem device. Gray line is the sum of both EQEs from the top and bottom cells.

Charge transport

To understand the impact on device performances with the different additives, we examined the electrical and charge transport properties of the perovskite films by time-resolved microwave conductivity (TRMC), conductive-atomic force microscopy (C-AFM), and vertical J - V measurements. In TRMC, the transient change in the density of mobile charge carriers photogenerated by a 5-ns pump-laser pulse was monitored through attenuation of an ~ 9 -GHz frequency microwave probe, which yielded information about free carrier mobility and lifetime (27–29). Figure 4A compares mobility transients measured at an absorbed photon flux of $\sim 1 \times 10^{10} \text{ cm}^{-2}$ using 640-nm laser excitation. By fitting the decay rate of the mobility yield product ($\phi \sum \mu$)—where ϕ is the carrier generation yield (usually near unity for high-quality perovskites) (28) and μ is the mobility for carriers—we determined the carrier lifetime, as indicated by the numerical values in Fig. 4A. All samples containing a PEA source had long lifetimes in the microsecond regime. The $\text{PEA}(\text{I}_{0.25}\text{SCN}_{0.75})$ sample, in particular, had the longest lifetime (approaching 3 μs). The $\text{PEA}(\text{I}_{0.25}\text{SCN}_{0.75})$ and PEASCN samples exhibited a high mobility product value ($>40 \text{ cm}^2 \text{ V}^{-1} \text{ s}^{-1}$), whereas the PEAI sample exhibited a relatively small value of $\sim 10 \text{ cm}^2 \text{ V}^{-1} \text{ s}^{-1}$. These mobility values were well maintained over a wide range of the excitation intensity (Fig. 4B).

To identify the factors affecting the various FFs of the samples with different ratios of anions in the PEA source (Fig. 1B), we investigated the electrical conductivity of different perovskite films by vertical dark J - V measurements using a structure consisting of ITO/perovskite/Au (Fig. 4C). When SCN was present, electrical conductivity was higher, which yielded a higher FF. We also performed C-AFM measurements to examine the spatial distribution of the current paths through the thickness of the perovskite films. Samples for

the C-AFM measurements were ITO/PTAA/perovskite, and current mapping was constructed by a Pt-Ir-coated tip at the sample bias of +1 V. For $\text{PEA}(\text{I}_{0.25}\text{SCN}_{0.75})$ (Fig. 4E) and PEASCN (Fig. 4F), the preferential current flow was through the grain boundaries with a relatively uniform contribution to the current through intragrain regions. The $\text{PEA}(\text{I}_{0.25}\text{SCN}_{0.75})$ sample exhibited slightly less grain-to-grain fluctuation than the PEASCN . In contrast, the PEAI sample (Fig. 4D) had a nonuniform current distribution, and many dead areas were visible. Dead regions in PEASCN and $\text{PEA}(\text{I}_{0.25}\text{SCN}_{0.75})$ samples were much fewer in number relative to those in the PEAI sample.

In imaging studies (Fig. 4, G to I), a feature was commonly found in the 2D phase, located at the grain boundaries of the film with $\text{PEA}(\text{I}_{0.25}\text{SCN}_{0.75})$ additives. Darker contrast in HAADF was observed in many regions within the 2D phase (blue arrows in Fig. 4G). Atomically resolved STEM images focusing on one of these dark regions (Fig. 4, H and I) revealed anomalies in the stacking of the 2D layers. Examples include (i) the insertion of an extra half-plane (i.e., edge dislocation), (ii) the merging or splitting of adjacent layers within a stack of PbI_2 (consisting of layers of I only, Pb only, and, again, I only), (iii) the bending of layers, and (iv) the interconnection between layers of PbI_2 . We speculate that the formation of these unusual planar defects stemmed from chemical inhomogeneity caused by local evaporation of SCN molecules, which are very volatile, during heat treatment (20). These planar defects could facilitate charge-conduction paths across 2D layers that would otherwise be difficult to achieve (30), and the defects both enhance charge collection (improving J_{SC}) and reduce the overall series resistance of the perovskite film (improving FF).

2T tandem solar cells

We used our wide-bandgap perovskite to fabricate 2T monolithic perovskite/Si tandem solar

cells. The Si bottom cell was textured only on the backside. On top of the Si bottom cell, the following stacking of layers was prepared: ITO as the recombination layer, PTAA, wide-bandgap perovskite, C_{60} , and polyethylenimine (PEIE) as not only an electron transport layer but also a buffer layer to minimize sputter damage during the subsequent ITO deposition (Fig. 5A). Further details about the tandem cell fabrication are provided in supplementary materials. The active area of the 2T tandem cell was 0.188 cm^2 , as defined by the aperture. The champion 2T tandem device achieved 26.7% PCE with a J_{SC} of 19.2 mA cm^{-2} , V_{OC} of 1.756 V, and FF of 0.792 with negligible hysteresis and a stabilized power output value $>26.5\%$ (Fig. 5B). Ideal spectral matching between the 1.68-eV perovskite and the 1.12-eV Si led to a $J_{\text{SC}} > 19 \text{ mA cm}^{-2}$. To verify our in-house measurement, a 2T tandem device of the same design with an active area of 1.001 cm^2 was certified with an efficiency of 26.2%. The official report is included in the supplementary materials (fig. S16).

In Fig. 5C, the EQE of the tandem device and the 1- R (reflectance) spectrum are presented. The current densities through the top and the bottom cell were consistent with the J_{SC} from the J - V curve. The separate contributions of the top perovskite and the bottom Si cells to the total V_{OC} of the tandem device were determined by Si cell measurement with light filtered by the perovskite top cell (31). The J - V curves of the light-filtered Si cell, as well as the unfiltered Si cell, are shown in fig. S15. The light-filtered Si cell has a 9.4% PCE with a V_{OC} of 0.62 V. Comparing the total V_{OC} of the 2T tandem device and the V_{OC} from the light-filtered Si bottom cell, we found that the gain in V_{OC} from the perovskite top cell was 1.132 V, or 64% of the total V_{OC} . This large contribution from the perovskite top cell exceeds that of other reported 2T perovskite/Si tandem cells with identified relative contributions of each cell (table S1). The high performance of our wide-bandgap perovskite cell validates the use of perovskites to potentially reach $>30\%$ PCE for Si-based tandems once the Si bottom cell is further optimized.

REFERENCES AND NOTES

1. National Renewable Energy Laboratory, "Best Research-Cell Efficiency Chart" (2019); www.nrel.gov/pv/cell-efficiency.html.
2. J. Tong et al., *Science* **364**, 475–479 (2019).
3. D. Kim et al., *J. Phys. Chem. C* **120**, 21330–21335 (2016).
4. S. R. Pae et al., *ACS Appl. Mater. Interfaces* **10**, 534–540 (2018).
5. Y. Rong et al., *Science* **361**, eaat8235 (2018).
6. J. P. Mailoa et al., *Appl. Phys. Lett.* **106**, 121105 (2015).
7. F. Sahli et al., *Nat. Mater.* **17**, 820–826 (2018).
8. B. Chen et al., *Joule* **3**, 177–190 (2019).
9. H. Shen et al., *Sci. Adv.* **4**, eaau9711 (2018).
10. M. Jošt et al., *Energy Environ. Sci.* **11**, 3511–3523 (2018).
11. T. Leijtens, K. A. Bush, R. Prasanna, M. D. McGehee, *Nat. Energy* **3**, 828–838 (2018).
12. E. T. Hoke et al., *Chem. Sci.* **6**, 613–617 (2015).
13. Z. Wang et al., *Nat. Energy* **2**, 17135 (2017).
14. Y. Liu et al., *Sci. Adv.* **5**, eaaw2543 (2019).

15. J.-W. Lee *et al.*, *Nat. Commun.* **9**, 3021 (2018).
16. M. Jung, T. J. Shin, J. Seo, G. Kim, S. I. Seok, *Energy Environ. Sci.* **11**, 2188–2197 (2018).
17. D. H. Kim *et al.*, *Joule* **3**, 1734–1745 (2019).
18. J. A. Christians *et al.*, *Nat. Energy* **3**, 68–74 (2018).
19. J. Xu *et al.*, *Science* **367**, 1097–1104 (2020).
20. X. Zhang *et al.*, *Adv. Energy Mater.* **8**, 1702498 (2018).
21. Y.-M. Kim *et al.*, *Nat. Mater.* **11**, 888–894 (2012).
22. H. J. Jung *et al.*, *Adv. Mater.* **30**, e1802769 (2018).
23. R. Ishikawa *et al.*, *Nat. Mater.* **10**, 278–281 (2011).
24. Q. Jiang *et al.*, *Nat. Photonics* **13**, 460–466 (2019).
25. Y. C. Kim *et al.*, *Adv. Energy Mater.* **6**, 1502104 (2016).
26. P. Fassl *et al.*, *Energy Environ. Sci.* **11**, 3380–3391 (2018).
27. O. G. Reid *et al.*, *J. Phys. D Appl. Phys.* **50**, 493002 (2017).
28. D. H. Kim *et al.*, *Adv. Mater.* **29**, 1606831 (2017).
29. O. Gunawan *et al.*, *Nature* **575**, 151–155 (2019).
30. A. Cröll, J. Tonn, E. Post, H. Böttner, A. Danilewsky, *J. Cryst. Growth* **466**, 16–21 (2017).
31. I. J. Park *et al.*, *Joule* **3**, 807–818 (2019).

ACKNOWLEDGMENTS

Funding: This work was supported by the National Research Foundation of Korea (NRF) funded by the Korean government's Ministry of Science and ICT (MSIT) (nos. NRF-2018R1A5A1025594, 2017R1A2B3010474, and 2020R1A2C3008111); the Korea Institute of Energy Technology Evaluation and Planning (KETEP) and the

Ministry of Trade, Industry and Energy (MOTIE) of the Republic of Korea (nos. 20183010014470 and 20193091010310); and the Nano-Material Technology Development Program (Green Nano Technology Development Program) through the NRF funded by the Ministry of Education, Science and Technology (nos. 2018M3A7B4065662 and 2019M3D1A2104109). The work at the National Renewable Energy Laboratory was supported by De-risking Halide Perovskite Solar Cells program of the National Center for Photovoltaics, funded by Office of Energy Efficiency and Renewable Energy, Solar Energy Technologies Office, U.S. Department of Energy (DOE) under contract no. DE-AC36-08G028308 with Alliance for Sustainable Energy, Limited Liability Company (LLC), the Manager and Operator of the National Renewable Energy Laboratory. The views expressed in the article do not necessarily represent the views of the DOE or the U.S. government. The U.S. government retains and the publisher, by accepting the article for publication, acknowledges that the U.S. government retains a nonexclusive, paid-up, irrevocable, worldwide license to publish or reproduce the published form of this work, or allow others to do so, for U.S. government purposes. This work made use of the EPIC facility of Northwestern University's NUANCE Center, which has received support from the Soft and Hybrid Nanotechnology Experimental (SHyNE) Resource (NSF ECCS-1542205); the MRSEC IRG2 program (NSF DMR-1720139) at the Materials Research Center; the International Institute for Nanotechnology (IIN); the Keck Foundation; and the State of Illinois, through the IIN. **Author contributions:** K.Z., D.H.K., and B.S. conceived the project; D.K., D.H.K., and B.S. designed the experiments

and characterizations; D.K. and D.H.K. prepared wide-bandgap perovskite samples and devices; H.J.J., D.K., and V.D. conducted TEM measurements and analysis; I.J.P., D.K., S.G.J., J.Y.K., and D.H.K. carried out the fabrication and characterization of 2T perovskite/Si tandem cells; B.W.L. conducted TRMC measurement; S.P.D. and J.T. conducted long-term stability measurements of wide-bandgap perovskite devices; C.X. conducted C-AFM measurements; D.K., F.Z., and S.G.J. conducted SEM measurements; D.K. and P.B. conducted XRD measurements; D.K., H.J.J., J.T., J.K., S.R.P., M.K., V.D., J.J.B., D.H.K., K.Z., and B.S. discussed the results and provided feedbacks for experiments; D.K., H.J.J., D.H.K., and B.S. wrote the manuscript; and all authors reviewed the manuscript and provided suggestions for edits. **Competing interests:** The authors declare no competing interests. **Data and materials availability:** All data are available in the main text or the supplementary materials.

SUPPLEMENTARY MATERIALS

science.sciencemag.org/content/368/6487/155/suppl/DC1
Materials and Methods
Figs. S1 to S16
Table S1
References (32–38)

27 November 2019; accepted 12 March 2020
Published online 26 March 2020
10.1126/science.aba3433